

# First-Principles Theory of Chirality-Induced Spin Selectivity at Molecule-Metal Interfaces in Photoemission

Amos Afugu, Gyanu P. Kafle, and Zhen-Fei Liu\*

*Department of Chemistry, Wayne State University, Detroit, Michigan 48202, USA*

E-mail: zfliu@wayne.edu

## Abstract

Spin-resolved photoelectron spectroscopy (PES) is a major experimental probe of chirality-induced spin selectivity (CISS), yet it remains unclear whether the measured spin polarization reflects molecular chirality itself or the broader electronic structure of the hybrid interface. We present a first-principles theory of PES spin polarization at chiral molecule-metal interfaces, treating the interface holistically rather than as a metal substrate plus a separate molecular spin filter/polarizer. Using density functional theory within a three-step photoemission framework, we compute the spin polarization generated in the optical-excitation step for (*M*)- and (*P*)-heptahelicene adsorbed on Au(111) and Cu(111), and for coronene/Au(111) as a non-chiral control. We find that adsorption strongly reshapes the PES spin polarization relative to the clean metal surface, but opposite enantiomers yield symmetry-related, qualitatively similar responses that are also comparable to that of the non-chiral coronene. These results indicate that changes in the PES spin polarization are more naturally attributed to the electronic structure of the hybrid interface than to molecular chirality alone.

Chirality-induced spin selectivity (CISS) is an emerging field that studies the coupling between chirality – a fundamental geometric property of molecules – and electron spin, an intrinsic quantum degree of freedom.<sup>1,2</sup> The term CISS encompasses a broad range of phenomena, including those observed in photoelectron spectroscopy (PES),<sup>3,4</sup> electron transport and tunneling,<sup>5,6</sup> and catalysis.<sup>7,8</sup> Among these, spin-resolved PES is often regarded as the gold standard for characterizing the CISS effect<sup>2</sup> and has been applied to both helical and point-chiral systems, such as DNA,<sup>9</sup> proteins,<sup>10</sup> heptahelicene,<sup>11,12</sup> helical tetrapyrrole,<sup>13</sup> methylcyclohexanone,<sup>14</sup> and chiral CuO thin film.<sup>15</sup> In these experiments, chiral molecules are adsorbed on a metal surface, and the spin polarization of photoelectrons emitted from the metal surface (more precisely, from the molecule-metal interface) is measured and compared to that of the clean metal surface without molecular adsorbates. Reported observations have often been interpreted in terms of a handedness-dependent change in photoelectron spin polarization, in some cases even on substrates with weak intrinsic spin-orbit coupling (SOC).<sup>10</sup> These findings call for a rigorous microscopic understanding of the origin of CISS effects reported in PES measurements, as well as a careful and critical assessment of the respective roles of the chiral molecule and the hybrid molecule-metal interface.

A variety of theoretical models have been advanced to rationalize these experimental findings,<sup>16</sup> including approaches based on scattering theory,<sup>17–21</sup> symmetry considerations,<sup>22,23</sup> electron correlation,<sup>24–26</sup> nonequilibrium dynamics,<sup>27–29</sup> and spinterface physics.<sup>30</sup> Despite these efforts, a comprehensive first-principles computational framework remains lacking. With the SOC treated at the *ab initio* level, the computed spin polarization is typically orders of magnitude smaller than experiments.<sup>31,32</sup> Notably, most prior first-principles studies have focused on CISS in electron transport below the vacuum level,<sup>33,34</sup> where the operative mechanisms differ fundamentally from those governing PES, which probes excited states above the vacuum level and involves distinct initial and final states. Consequently, methods developed to explain CISS in transport measurements may not be directly transferable to PES. Furthermore, many existing treatments conceptually separate the chiral molecular ad-

sorbate from the metal substrate, emphasizing either spin-filtering<sup>18,35</sup> or spin-polarizing<sup>36</sup> effects within the molecular layer on the electron flow originating from the metal. Such a viewpoint overlooks the central role of the molecule-metal interface, neglecting both the adsorbate-induced modification of the metal electronic structure and emergent interfacial states arising from the molecule-metal hybridization.

In this work, we treat the molecule-metal interface holistically as the relevant microscopic object. Within this picture, the change in photoelectron spin polarization is not attributed solely to the molecular layer, but rather emerges from the hybridized interface, where adsorbate-induced modulation of the metal states gives rise to spin-dependent photoemission different from that of the clean metal surface. We believe this viewpoint highlights interfacial states as the central mediators that naturally connect the intrinsic large SOC in the metal to the spin polarization in PES. We compute PES intensities using a three-step model<sup>37,38</sup> and focus our discussion on the first step, i.e., the optical excitation that involves initial and final states of the interface, as well as their spin texture and the polarization of the incident light. We isolate this step to identify qualitative trends, and defer the effects associated with the other two steps (transport and escape) and a more realistic final-state description to future work. For conceptual clarity, we employ an independent-particle description in which both the initial and final states are approximated by Kohn-Sham spinors computed from density functional theory (DFT). This approximation does not include all many-body and final-state effects, but it provides a controlled first-principles framework for identifying which features of the PES spin polarization are already encoded in the hybridized interface. Later in the paper, we also assess the effect of many-body corrections on the interfacial level alignment.<sup>39</sup>

Within the three-step photoemission model and the independent-particle approximation, the first step corresponds to an optical transition from an occupied initial state to an unoccupied final state. When the final state is non-degenerate, the transition probability is given

by Fermi's golden rule,

$$\mathcal{P}_{\text{fi}} \propto |\langle \phi_{\text{f}} | \mathbf{A} \cdot \mathbf{p} | \phi_{\text{i}} \rangle|^2 \delta(\epsilon_{\text{f}} - \epsilon_{\text{i}} - h\nu) \delta(E_{\text{kin}} - [\epsilon_{\text{f}} - E_{\text{vac}}]). \quad (1)$$

Here, the first factor is the optical transition matrix element, where  $\phi_{\text{i}}$  and  $\phi_{\text{f}}$  denote the (non-interacting) initial and final states, respectively. They are approximated in this work by Kohn-Sham orbitals obtained from DFT, which are two-component spinors.  $\mathbf{A}$  is the vector potential of the incident light, and  $\mathbf{p}$  is the momentum operator. Within the dipole approximation, the light-matter coupling reduces to  $\mathbf{A} \cdot \mathbf{p} = A_0(p_x \pm ip_y)$  in the velocity gauge for circularly polarized light. Here,  $A_0$  is a constant prefactor, and “+” corresponds to right circular polarization, defined for the direction of rotation of the electric vector being clockwise when viewed against the direction of light propagation. The “−” sign corresponds to left circular polarization. The first delta function in Eq. (1) enforces energy conservation during the optical excitation, with  $\epsilon_{\text{i}}$  and  $\epsilon_{\text{f}}$  denoting the Kohn-Sham eigenvalues of the initial and final states, respectively, and  $h\nu$  the photon energy. The second delta function in Eq. (1) enforces energy conservation upon electron escape into vacuum, where  $E_{\text{kin}}$  is the kinetic energy of the emitted photoelectron and  $E_{\text{vac}}$  is the vacuum level.

When the final states form a degenerate manifold, transitions from a given initial state to different final states within that manifold interfere coherently.<sup>40,41</sup> Within a degenerate subspace  $\mathcal{D}$ , we therefore construct the optically excited state as

$$\begin{aligned} |\phi_{\text{i} \rightarrow \text{f}'} \rangle &= \sum_{j \in \mathcal{D}} p_{\text{i} \rightarrow \text{f}_j} |\phi_{\text{f}_j} \rangle \\ &= \sum_{j \in \mathcal{D}} (\langle \phi_{\text{f}_j} | p_x \pm ip_y | \phi_{\text{i}} \rangle) |\phi_{\text{f}_j} \rangle. \end{aligned} \quad (2)$$

Here, the transition amplitude is  $p_{\text{i} \rightarrow \text{f}_j} = \langle \phi_{\text{f}_j} | p_x \pm ip_y | \phi_{\text{i}} \rangle$  for circularly polarized light. It is worth noting that when the Hamiltonian  $\hat{H}$  contains nonlocal terms due to the pseudopotential – as is the case in our calculations – the physically relevant transition matrix elements

that we actually compute are those of the velocity operator,  $\langle \phi_f | \mathbf{v} | \phi_i \rangle$  with  $i\hbar\mathbf{v} = [\mathbf{r}, \hat{H}]$ , rather than those of the canonical momentum operator. The spin polarization along the  $z$  direction is defined as:

$$\zeta_z(\mathbf{K}_{\parallel}) = \frac{I_{\mathbf{K}_{\parallel}}(|S_z \uparrow\rangle) - I_{\mathbf{K}_{\parallel}}(|S_z \downarrow\rangle)}{I_{\mathbf{K}_{\parallel}}(|S_z \uparrow\rangle) + I_{\mathbf{K}_{\parallel}}(|S_z \downarrow\rangle)} \times 100\%. \quad (3)$$

In this equation,  $\mathbf{K}_{\parallel}$  denotes the in-plane momentum of the photoelectrons.  $I_{\mathbf{K}_{\parallel}}(|S_z \uparrow\rangle)$  denotes the probability of detecting the photoelectron with in-plane momentum  $\mathbf{K}_{\parallel}$  in the eigenstate  $|S_z \uparrow\rangle$  of  $\hat{S}_z$  with eigenvalue  $\hbar/2$ . Generalizing Fermi's golden rule in Eq. (1), this probability is given by

$$I_{\mathbf{K}_{\parallel}}(|S_z \uparrow\rangle) = \sum_i \sum_{f'} \|\langle S_z \uparrow | \phi_{i \rightarrow f'} \rangle\|^2 \delta(\epsilon_{f'} - \epsilon_i - h\nu) \times \delta(E_{\text{kin}} - [\epsilon_{f'} - E_{\text{vac}}]) \delta(\mathbf{K}_{\parallel} - \mathbf{k}_{\parallel} - \mathbf{G}_{\parallel}), \quad (4)$$

where the sums run over all occupied initial states and all degenerate final-state manifolds. The first factor represents the squared norm of the spatial component of the excited spinor  $|\phi_{f'}\rangle$  after projection onto  $|S_z \uparrow\rangle$ . The last delta function enforces conservation of in-plane momentum,<sup>37</sup> where  $\mathbf{k}_{\parallel}$  and  $\mathbf{G}_{\parallel}$  are the in-plane crystal momentum and reciprocal-space lattice vector in the Bloch wavefunctions. Technically, this is implemented such that we truncate the spinor  $|\phi_{i \rightarrow f'}\rangle = |\phi_{i \rightarrow f'}^{\alpha}\rangle |S_z \uparrow\rangle + |\phi_{i \rightarrow f'}^{\beta}\rangle |S_z \downarrow\rangle$  to certain plane-wave components:

$$\begin{aligned} |\phi_{i \rightarrow f'}^{\alpha}\rangle &= e^{i\mathbf{k}_{\parallel} \cdot \mathbf{r}} \sum_{\mathbf{G}} c_{\mathbf{G}}^{\alpha} e^{i\mathbf{G} \cdot \mathbf{r}} \\ &\rightarrow e^{i\mathbf{k}_{\parallel} \cdot \mathbf{r}} \sum_{G_z > 0} \sum_{\mathbf{G}_{\parallel} = \mathbf{K}_{\parallel} - \mathbf{k}_{\parallel}} c_{\mathbf{G}}^{\alpha} e^{i\mathbf{G} \cdot \mathbf{r}}. \end{aligned} \quad (5)$$

This is written for  $|\phi_{i \rightarrow f'}^{\alpha}\rangle$  and a similar treatment for  $|\phi_{i \rightarrow f'}^{\beta}\rangle$  applies. In the second line of Eq. (5), we restrict the summation to  $G_z > 0$  because only those plane-wave components can escape from the surface. In this work, we only consider  $\mathbf{K}_{\parallel}$  values that match our  $\mathbf{k}_{\parallel}$

sampling in the calculation, such that the second summation can be restricted to  $\mathbf{G}_{\parallel} = 0$  in these special cases.

Analogous definitions apply for  $\zeta_x$  and  $\zeta_y$ , or more generally for spin polarization along an arbitrary quantization axis. Equivalently, Eq. (3) can be expressed in density-matrix form as  $\text{Tr}(\rho\sigma_z)/\text{Tr}\rho$ , where  $\sigma_z$  is a Pauli matrix and  $\rho = \sum_i \sum_{f'} |\phi_{i \rightarrow f'}\rangle \langle \phi_{i \rightarrow f'}|$  is the spin density matrix of the photoexcited states. This formulation has been employed in the analysis of the spin polarization of photoelectrons from nonmagnetic solids and surfaces, including Au.<sup>42–44</sup>

In this work, we compute both in-plane spin polarizations  $\zeta_x^{\pm}$  and  $\zeta_y^{\pm}$ , and the out-of-plane component,  $\zeta_z^{\pm}$ , the latter being the quantity most commonly reported in experimental studies.<sup>9,11</sup> The superscript “ $\pm$ ” corresponds to the helicities of circularly polarized light introduced in Eq. (2). As follows from Eqs. (4), all spin polarization components depend explicitly on the kinetic energy  $E_{\text{kin}}$  of the emitted photoelectrons. We therefore present  $\zeta(E_{\text{kin}})$  throughout, noting that the maximum accessible  $E_{\text{kin}}$  is constrained by energy conservation to  $h\nu$  minus the surface work function. We evaluate the spin polarization both at the  $\Gamma$  point of the surface Brillouin zone and at finite  $\mathbf{k}_{\parallel}$  points away from  $\Gamma$ . The former corresponds to normal-emission PES measurements commonly performed in the literature,<sup>9,11</sup> although some experiments do report  $\mathbf{k}_{\parallel}$ -resolved spin polarization.<sup>12</sup> In all calculations, the first two delta functions in Eq. (4) for energy conservation are approximated by Lorentzians:  $\delta(x_1 - x_2) \approx \gamma/[(x_1 - x_2)^2 + \gamma^2]$  with  $\gamma = 0.01$  eV.

We apply this theoretical framework to investigate the spin polarization of photoelectrons emitted from a series of molecule-metal interfaces shown in Figure 1. Specifically, we consider the chiral molecules (*M*)-heptahelicene (*M*-[7]H,  $\text{C}_{30}\text{H}_{18}$ , *M* denoting minus helicity) and (*P*)-[7]H (*P* denoting plus helicity) adsorbed on Au (111), as shown in Figure 1(a) and (b), respectively. These systems correspond to those examined experimentally in Ref. 11. As a non-chiral control, we additionally study coronene ( $\text{C}_{24}\text{H}_{12}$ ) adsorbed on Au (111), shown in Figure 1(c). We choose this system due to its comparable lateral size and conjugation length to [7]H: it consists of seven peri-fused benzene rings, analogous to the seven annulated

benzene units in [7]H, but lacks intrinsic chirality. To further assess the role of substrate SOC, we also investigate (*M*)-[7]H and (*P*)-[7]H adsorbed on Cu (111), as shown in Figure 1(d) and (e), respectively. These systems were studied experimentally in Ref. 12. This combination of systems enables us to disentangle three effects: the intrinsic response of the clean substrate, the modification induced by adsorption of molecules, and the portion of that modification that is genuinely specific to molecular chirality. We primarily use  $h\nu = 5.83$  eV as the energy of the incident light in the calculations (consistent with experiment<sup>11,12</sup>) and also report results using other photon energies in the Supporting Information.

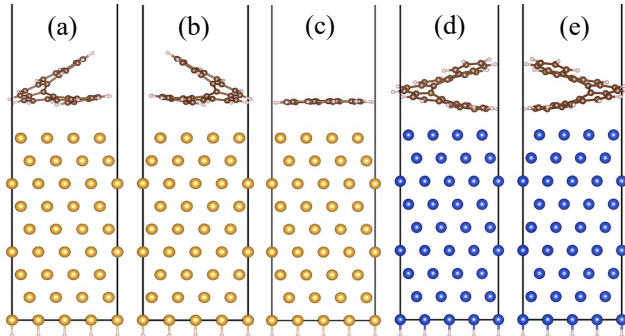


Figure 1: Interfaces studied in this work. (a) (*M*)-[7]H, (b) (*P*)-[7]H, and (c) coronene adsorbed on Au (111). (d) (*M*)-[7]H and (e) (*P*)-[7]H adsorbed on Cu (111). The bottom metal surface is passivated with hydrogen atoms.

In Figure 1, the Au (111) and Cu (111) substrates are modeled using nine-layer slabs, each consisting of a  $4 \times 4$  lateral supercell of Au or Cu atoms. The equivalent bulk lattice constants are 4.08 Å for Au and 3.61 Å for Cu, in good agreement with experimental values. The choice of nine layers reflects the minimal slab thickness required to produce a finite spin splitting of the surface states for clean Au (111). An accurate description of the surface states is essential for the present study: in typical PES measurements probing CISS,<sup>9</sup> the photon energy is  $h\nu = 5.83$  eV, which, given the Au (111) work function of approximately 5.3 eV,<sup>45</sup> restricts the accessible binding energies to within 1 eV below the Fermi level. In this narrow energy window, the spin texture of the surface states constitutes a primary source of spin polarization.<sup>46,47</sup> Moreover, to eliminate spurious contributions from the opposite side of the slab, the bottom metal surface is passivated with hydrogen atoms, thereby suppressing

artificial surface states and ensuring that the calculated PES response originates solely from the molecule-metal interface of interest.

Details of the geometry optimization are provided in the Supporting Information. We explicitly relax the (*M*)-[7]H/Au, coronene/Au, and (*M*)-[7]H/Cu interfaces, while the corresponding (*P*)-[7]H interface structures are generated by taking the mirror image of the (*M*)-[7]H configurations with respect to the *xz* plane. This ensures that any differences observed between the two enantiomers arise from electronic effects rather than from geometry variations.

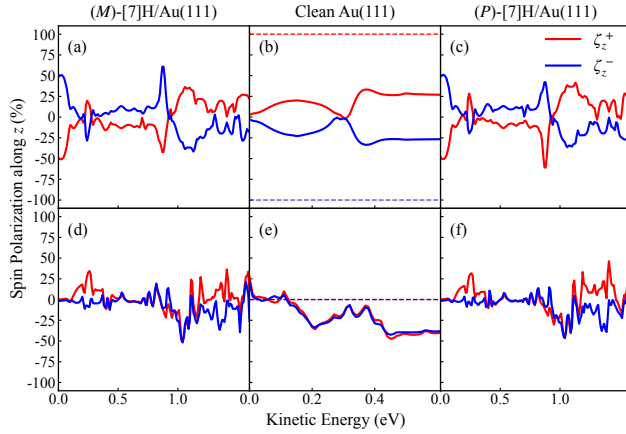


Figure 2: Spin polarization along the *z* direction. (a)(d) (*M*)-[7]H adsorbed on Au (111). (b)(e) Clean Au (111), where dashed lines are computed for a nine-layer unit cell and solid lines are computed for an Au slab with coordinates adopted from the (*M*)-[7]H/Au interface. (c)(f) (*P*)-[7]H adsorbed on Au (111). (a-c) Computed at the  $\Gamma$  point. (d-f) Computed at  $\mathbf{k}_{\parallel} = (0, 0.03333)$ , expressed in fractional coordinates of the in-plane reciprocal lattice vectors. In all panels, red (blue) lines denote  $\zeta_z^+$  ( $\zeta_z^-$ ), spin polarization under right (left) circularly polarized light.

We begin with the clean Au (111) surface in the absence of molecular adsorbates. Figure 2(b) presents the out-of-plane spin polarization at the  $\Gamma$  point,  $\zeta_z^{\pm}(E_{\text{kin}})$ , under right (“+”) and left (“-”) circularly polarized light with photon energy  $h\nu = 5.83$  eV. For comparison, in Figure 2(e), we show the same quantities evaluated at  $\mathbf{k}_{\parallel} = (0, 0.03333)$  in fractional coordinates of the in-plane reciprocal lattice vectors of the interface. We select this  $\mathbf{k}_{\parallel}$  point because  $|\mathbf{k}_{\parallel}| = 0.02 \text{ \AA}^{-1}$  corresponds to an acceptance angle of approximately  $\theta \sim 2.3^\circ$  for photoelectrons with  $E_{\text{kin}} \sim 1$  eV in a typical PES measurement, as estimated from

$|\mathbf{k}_{\parallel}| = \sqrt{2E_{\text{kin}}}\sin\theta$  (in atomic units). In both panels, dashed lines denote results obtained using a nine-layer Au (111) unit cell, whereas solid lines correspond to a  $4 \times 4 \times 9$  Au (111) slab with the atomic coordinates adopted from the relaxed (*M*)-[7]H/Au interface system. The difference between dashed and solid curves arises exclusively from geometry relaxation of the molecule-metal interface, as calculations performed for a fully periodic  $4 \times 4 \times 9$  Au (111) supercell without molecular adsorbates simply reproduce the results of the nine-layer Au (111) unit cell.

The spin polarization of the Au (111) unit cell reflects both the symmetry of the surface and the specific photon energy used. At  $h\nu = 5.83$  eV, we find  $\zeta_z^{\pm} = \pm 1$  at the  $\Gamma$  point. Figure S2 of the Supporting Information summarizes the behaviors of  $\zeta_x^{\pm}$ ,  $\zeta_y^{\pm}$ , and  $\zeta_z^{\pm}$  at four additional representative  $\mathbf{k}_{\parallel}$  points in the vicinity of  $\Gamma$ . We select those  $\mathbf{k}_{\parallel}$  points of the unit cell again because they satisfy  $|\mathbf{k}_{\parallel}| = 0.02 \text{ \AA}^{-1}$ . As  $\mathbf{k}_{\parallel}$  moves away from  $\Gamma$ , the out-of-plane component  $\zeta_z^{\pm}$  vanishes. At  $\Gamma$ , both in-plane components  $\zeta_x^{\pm}$  and  $\zeta_y^{\pm}$  vanish by symmetry. More generally,  $\zeta_x^{\pm} = 0$  along the  $k_x$  axis and  $\zeta_y^{\pm} = 0$  along the  $k_y$  axis of the reciprocal space. Along the reciprocal lattice vectors  $\mathbf{b}_1$  and  $\mathbf{b}_2$ , we further find  $\zeta_x^+ = \zeta_x^-$  and  $\zeta_y^+ = \zeta_y^-$ , suggesting vanishing circular dichroism, in agreement with Ref. 48. For  $h\nu = 5.83$  eV, the photoemission process involves only the Shockley surface states located approximately 0.5 eV below the Fermi level, which are doubly degenerate at  $\Gamma$  (Kramers degeneracy) and spin split at all other  $\mathbf{k}_{\parallel}$  points. When a larger photon energy is used, additional initial states contribute. As shown in Figure S3 of the Supporting Information, for  $h\nu = 8$  eV and 10 eV,  $\zeta_z^{\pm}$  at  $\Gamma$  is reduced below unity, which we attribute to destructive interference among transitions originating from multiple initial states.

This idealized behavior is strongly reduced once the Au geometry is taken from the relaxed molecule-metal interface, even after removing the molecule. Figure 2(b)(e) present the results for the  $4 \times 4 \times 9$  Au (111) slab whose atomic coordinates are adopted from the relaxed (*M*)-[7]H/Au interface, where we observe qualitative changes in the spin polarization compared to the primitive Au (111) unit cell. The calculated work function of this slab is

5.20 eV, implying that the incident light with  $h\nu = 5.83$  eV can probe electronic states up to 0.63 eV below the Fermi level. At the  $\Gamma$  point, the out-of-plane spin polarization  $\zeta_z^\pm$  decreases from unity to about 20%, with  $\zeta_z^+ = -\zeta_z^-$  for all  $E_{\text{kin}}$ . In contrast, at  $\mathbf{k}_\parallel = (0, 0.03333)$ ,  $\zeta_z^\pm$  becomes finite, with  $\zeta_z^+ \neq \zeta_z^-$ . This change can be understood as a consequence of symmetry lowering and the associated mixing of irreducible representations in the initial and/or final states.<sup>44</sup> The comparison therefore suggests that even modest departures from perfect surface symmetry can strongly alter the computed PES spin polarization. This needs to be taken into account when connecting theory to experiment. Rather than taking the ideal  $\zeta_z^\pm = \pm 1$  result as the relevant experimental baseline, the lesson is that the spin polarization of Au(111) is highly sensitive to the actual local geometry of the interface. Small random distortions on top of a perfect Au (111) slab lead to the same qualitative conclusion.

We next consider (*M*)-[7]H and (*P*)-[7]H adsorbed on Au (111). Molecular adsorption lowers the work function to 4.22 eV. Consequently, for incident light with  $h\nu = 5.83$  eV, the maximum kinetic energy of the emitted electrons is  $E_{\text{kin}} = 1.61$  eV. Figures 2(a) and (c) show the  $\zeta_z^\pm$  results for the (*M*)-[7]H/Au and (*P*)-[7]H/Au interfaces, respectively, at the  $\Gamma$  point, while Figures 2(d) and (f) present the corresponding results at  $\mathbf{k}_\parallel = (0, 0.03333)$ .  $\zeta_x^\pm$  and  $\zeta_y^\pm$  results at  $\Gamma$  are presented in Figure S4 of the Supporting Information. Compared to the clean Au (111) surface, the adsorption of the chiral molecules substantially modifies the energy-resolved spin polarization. In the presence of molecular adsorbates, Kramers degeneracy remains at  $\Gamma$  while spin splitting appears away from  $\Gamma$ .

To determine whether these changes are genuinely enantiomer specific, we analyze the symmetry relation between the two helicene/Au interfaces. After a careful symmetry analysis of the data for all  $\mathbf{k}_\parallel$  points considered in the Brillouin zone, we find that the following

relations hold:

$$\zeta_x^\pm(M; k_x, k_y) = -\zeta_x^\mp(P; k_x, -k_y); \quad (6a)$$

$$\zeta_y^\pm(M; k_x, k_y) = \zeta_y^\mp(P; k_x, -k_y); \quad (6b)$$

$$\zeta_z^\pm(M; k_x, k_y) = -\zeta_z^\mp(P; k_x, -k_y). \quad (6c)$$

These relations arise because the  $(M)$ -[7]H/Au and  $(P)$ -[7]H/Au systems are related by a mirror reflection with respect to the  $xz$  plane, which maps  $k_y \rightarrow -k_y$  and transforms the spin polarizations accordingly. In addition, the definitions of the  $x$  and  $y$  directions (see Figure S1 of the Supporting Information), as well as the molecular orientations on the surface, must be taken into account when interpreting the in-plane spin polarization. In contrast, the out-of-plane component of the spin polarization is the most straightforward quantity for the present comparison and is also the quantity often measured in experiment. In particular, at the  $\Gamma$  point (corresponding to normal emission in PES), symmetry requires that  $\zeta_z^\pm(M) = -\zeta_z^\mp(P)$ . Thus, within the present theoretical framework, the two enantiomers are not expected to produce independent normal-emission responses; rather, their  $\Gamma$ -point signals are symmetry linked. Any enantiomer-dependent asymmetry in  $\zeta_z$  can only appear away from  $\Gamma$ .

This symmetry analysis clarifies the main trend in Figure 2. Although the two enantiomers –  $(M)$ -[7]H and  $(P)$ -[7]H – modify the spin polarization of photoelectrons emitted from the Au (111) surface, their effects are qualitatively similar and symmetry related. In other words, within the present first-principles treatment, the dominant effect of adsorption on Au (111) is to reshape the interfacial photoemission response, rather than generating a large, systematic, enantiomer-dependent shift in the out-of-plane spin polarization. This conclusion is qualitatively consistent with Ref. 12 and is less supportive of interpretations that attribute every adsorbate-induced change in PES spin polarization directly to chirality alone.

The key question is whether the changes found for helicene/Au interfaces arise specifically

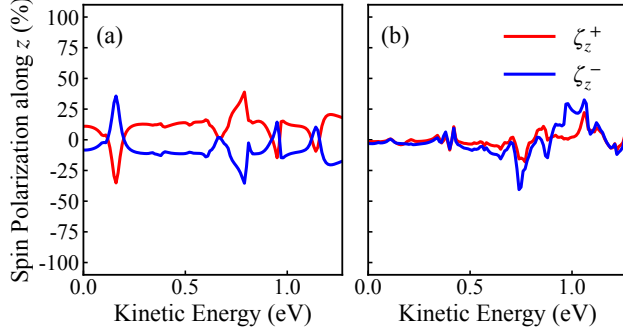


Figure 3: Spin polarization along the  $z$  direction, for coronene adsorbed on Au (111), at (a) the  $\Gamma$  point and (b)  $\mathbf{k}_{\parallel} = (0, 0.03333)$ , expressed in fractional coordinates of the in-plane reciprocal lattice vectors. In both panels, red (blue) lines denote  $\zeta_z^+$  ( $\zeta_z^-$ ), spin polarization under right (left) circularly polarized light.

from chirality, or whether similar changes can result more generally from adsorption-induced modification of the interface. To address this question, we examine a non-chiral control system, coronene adsorbed on Au (111), as shown in Figure 1(c). This interface has a work function of 4.54 eV, leading to the maximum  $E_{\text{kin}}$  being 1.29 eV for an incident light with  $h\nu = 5.83$  eV. The corresponding out-of-plane spin polarization,  $\zeta_z^{\pm}$ , is computed at the  $\Gamma$  point and at  $\mathbf{k}_{\parallel} = (0, 0.03333)$ , as presented in Figure 3(a) and (b), respectively. The symmetry of the non-chiral interface enforces  $\zeta_z^+ = -\zeta_z^-$  at  $\Gamma$ , while Eq. (6) constrains how the two enantiomers map onto one another. As seen from these results, coronene induces changes in  $\zeta_z^{\pm}$  that are qualitatively similar to those produced by either (*M*)-[7]H or (*P*)-[7]H, both at  $\Gamma$  and at finite  $\mathbf{k}_{\parallel}$ . This similarity shows that substantial adsorbate-induced changes in PES spin polarization are not necessarily tied to the chirality of the adsorbate. For the same incident light energy, the lowered work function at the molecule-metal interface enables more occupied states to contribute to PES, including hybridized molecule-metal states. Together with the associated changes in the transition matrix elements, this provides a natural explanation for why non-chiral and chiral adsorbates can produce qualitatively similar modifications.

To further probe the role of substrate SOC, we investigate (*M*)-[7]H and (*P*)-[7]H adsorbed on Cu (111), a system examined experimentally in Ref. 12. The results are shown in

Figure 4, presented in the same format as Figure 2 for the Au-based systems. The clean Cu (111) slab, with coordinates adopted from the (*M*)-[7]H/Cu interface, has a work function of 4.76 eV. Owing to the weak intrinsic SOC in Cu, it exhibits negligible out-of-plane spin polarization. Upon adsorption of the chiral molecules, the work function is reduced to 3.60 eV, implying the maximum  $E_{\text{kin}}$  is 2.23 eV for an incident light with  $h\nu = 5.83$  eV. For the interfaces,  $\zeta_z^\pm$  is modified to a moderate extent; however, its average over the accessible  $E_{\text{kin}}$  range remains close to zero. Moreover, the symmetry relations expressed in Eq. (6) continue to hold, as expected from the same mirror relationship between the two geometries.

These results on Cu-based interfaces reinforce two points. First, they support the interpretation that the large SOC of Au is an important ingredient in generating a sizable PES spin polarization at the interface. Second, even when the chiral adsorbate is present, the computed response on Cu remains much smaller than on Au, again emphasizing that the molecule cannot be viewed as the sole source of the photoemission spin polarization. Overall, our results are consistent with the findings of Ref. 12, while also suggesting that stronger effects reported for other surfaces, such as Cu (332),<sup>11</sup> likely depend sensitively on the detailed interface geometry and measurement conditions.

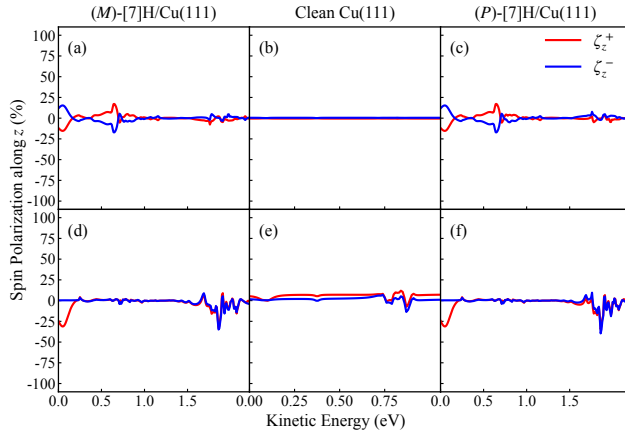


Figure 4: Spin polarization along the  $z$  direction. (a)(d) (*M*)-[7]H adsorbed on Cu (111). (b)(e) Clean Cu (111) slab with coordinates adopted from the (*M*)-[7]H/Cu interface. (c)(f) (*P*)-[7]H adsorbed on Cu (111). (a-c) Computed at the  $\Gamma$  point. (d-f) Computed at  $\mathbf{k}_{\parallel} = (0, 0.03333)$ , expressed in fractional coordinates of the in-plane reciprocal lattice vectors. In all panels, red (blue) lines denote  $\zeta^+$  ( $\zeta^-$ ), spin polarization under right (left) circularly polarized light. This figure is analogous to Figure 2, but for the Cu-based systems.

All results presented thus far are based on DFT electronic structures. Here, we briefly assess the impact of many-body corrections, focusing on improved level alignment at the molecule-metal interface.<sup>39</sup> Figure 5(a) shows the band structure of the (*M*)-[7]H/Au interface, with bands color-coded by their projected character. This calculation employs the Perdew-Burke-Ernzerhof (PBE) functional<sup>49</sup> with SOC and includes four Au (111) layers to reduce the computational cost. At the  $\Gamma$  point, we observe appreciable hybridization between molecular orbitals and Au states. In particular, the projected HOMO of (*M*)-[7]H lies approximately 0.92 eV below the Fermi level. The reduced work function at the interface implies that incident light with  $h\nu = 5.83$  eV probes states up to 1.56 eV below the Fermi level, thereby encompassing these hybridized states. Given the well-known tendency of PBE to underestimate interfacial level alignment,<sup>50</sup> we further perform first-principles  $G_0W_0$ @PBE calculations<sup>51,52</sup> to obtain a more accurate electronic structure, shown in Figure 5(b), with computational details provided in the Supporting Information. At the *GW* level, the HOMO is shifted to 1.23 eV below the Fermi level, but remains within the energy window accessible in PES. We also note that the Au *d* states, located around 2 eV below the Fermi level, lie outside this energy window and therefore do not contribute to the photoemission signal considered here. This supports the conclusion that corrections in the level alignment alone do not overturn the qualitative interface-based interpretation developed from the DFT results.

Several limitations of the present approach should be kept in mind. Our treatment focuses on the first step (optical excitation) of the three-step photoemission model and employ an independent-particle description of the optical excitation. This framework is useful for identifying qualitative trends controlled by the hybridized interface, but it does not yet include all effects needed for a quantitatively complete comparison with experiment. In particular, we do not include the matrix-element renormalization beyond the independent-particle picture, the more realistic final-state description used in one-step photoemission theory<sup>53</sup> (treating the final state as a time-reversed low-energy electron diffraction state), electron-vibrational coupling, or structural order/disorder. These factors may be important when making a de-

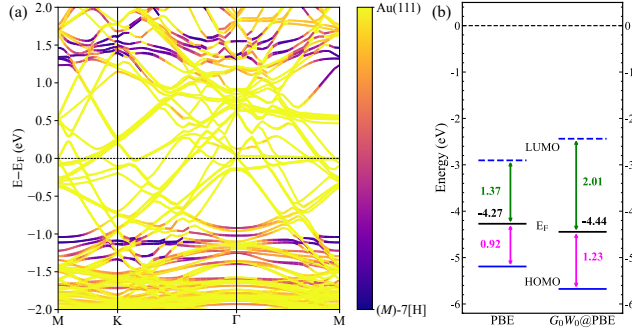


Figure 5: Electronic structure of the  $(M)$ -[7]H/Au interface that includes four layers of Au (111). (a) PBE band structure, with color denoting the projected character of each orbital. Fermi level of the interface is set to be zero. (b) PBE and  $G_0W_0@PBE$  energy level alignment at the  $\Gamma$  point. Solid and dashed blue lines represent the highest occupied molecular orbital (HOMO) and the lowest unoccupied molecular orbital (LUMO) of the  $(M)$ -7[H], respectively. Black lines represent the Fermi level of the interface. Vacuum level is set to be zero.

tailed comparison with experiment, especially because the spin polarization strongly depends on the chosen spin-analysis axis (in-plane vs. out-of-plane), kinetic energy of photoelectrons, crystal momentum, and the set of initial states contributing to the signal (or equivalently, the energy of incident light). From an experimental perspective, spin polarization might be sensitive to the acceptance angle, sample quality, atomic-scale interface structure, and precise data-processing procedure.

In summary, we developed a first-principles framework for spin polarization in photoemission from molecule-metal interfaces and applied it to helicene adsorbed on Au (111) and Cu (111), with coronene/Au as a non-chiral control. Within the present theory, we do not find a robust enantiomer-dependent enhancement or suppression of the spin polarization, but rather an adsorbate-induced modification of the interfacial photoemission response that is qualitatively similar for the two enantiomers, consistent with Ref. 12. Moreover, a non-chiral adsorbate induces comparable changes in the PES spin polarization, demonstrating that adsorbate-induced modification of the interface can mimic features that might otherwise be assigned to chirality alone. The apparent discrepancy with experiments that inferred stronger chirality-dependent effects may not necessarily indicate a fundamental inconsistency between theory and experiment. Rather, it may reflect, at least in part, the difficulty

of disentangling genuine enantiomer-specific signals from the effects of the molecule-metal interface, as well as the need for a more refined interpretation of the experimental observables, because changes attributed to molecular chirality can also arise from interface-induced electronic structure.

## Supporting Information Description

Orientations of the real- and reciprocal-space lattice vectors and the 2D Brillouin zone; spin polarization of Au (111) unit cell at different representative  $\mathbf{k}_{\parallel}$  points; spin polarization of Au (111) unit cell along the  $z$  direction using different energies of incoming light; spin polarization of (*M*)-7[H]/Au and (*P*)-7[H]/Au interfaces along the  $x$  and  $y$  directions at the  $\Gamma$  point; computational details of geometry optimization; computational details of  $G_0W_0$  calculations.

## Acknowledgments

We thank Thomas Frederiksen, Per Hedegård, Jeff Neaton, Latha Venkataraman, and Binghai Yan for fruitful discussions. This work is supported by an NSF CAREER award, DMR-2044552 and used Bridges-2 at the Pittsburgh Supercomputing Center through Allocation No. PHY220043 from the Advanced Cyberinfrastructure Coordination Ecosystem: Services & Support (ACCESS) program, which is supported by NSF Grants No. 2138259, No. 2138286, No. 2138307, No. 2137603, and No. 2138296. Very large-scale calculations were carried out using resources of the National Energy Research Scientific Computing Center, a DOE Office of Science User Facility supported by the Office of Science of the U.S. Department of Energy under Contract No. DE-AC02-05CH11231 using NERSC award BES-ERCAP0036533. Z.-F.L. acknowledges an Alfred P. Sloan Research Fellowship, No. FG-2024-21750.

## References

- (1) Naaman, R.; Paltiel, Y.; Waldeck, D. H. Chiral Molecules and the Electron Spin. *Nat. Rev. Chem.* **2019**, *3*, 250–260.
- (2) Bloom, B. P.; Paltiel, Y.; Naaman, R.; Waldeck, D. H. Chiral Induced Spin Selectivity. *Chem. Rev.* **2024**, *124*, 1950–1991.
- (3) Ray, K.; Ananthavel, S. P.; Waldeck, D. H.; Naaman, R. Asymmetric Scattering of Polarized Electrons by Organized Organic Films of Chiral Molecules. *Science* **1999**, *283*, 814–816.
- (4) Möllers, P. V. .; Göhler, B.; Zacharias, H. Chirality Induced Spin Selectivity – the Photoelectron View. *Isr. J. Chem.* **2022**, *62*, e202200062.
- (5) Xie, Z.; Markus, T. Z.; Cohen, S. R.; Vager, Z.; Gutierrez, R.; Naaman, R. Spin Specific Electron Conduction through DNA Oligomers. *Nano Lett.* **2011**, *11*, 4652–4655.
- (6) Albro, J. A.; Garrett, N. T.; Govindaraj, K.; Bloom, B. P.; Rosi, N. L.; Waldeck, D. H. Measurement Platform to Probe the Mechanism of Chiral-Induced Spin Selectivity through Direction-Dependent Magnetic Conductive Atomic Force Microscopy. *ACS Nano* **2025**, *19*, 17941–17949.
- (7) Mtangi, W.; Kiran, V.; Fontanesi, C.; Naaman, R. Role of the Electron Spin Polarization in Water Splitting. *J. Phys. Chem. Lett.* **2015**, *6*, 4916–4922.
- (8) Mondal, P. C.; Fontanesi, C.; Waldeck, D. H.; Naaman, R. Field and Chirality Effects on Electrochemical Charge Transfer Rates: Spin Dependent Electrochemistry. *ACS Nano* **2015**, *9*, 3377–3384.
- (9) Göhler, B.; Hamelbeck, V.; Markus, T. Z.; Kettner, M.; Hanne, G. F.; Vager, Z.; Naaman, R.; Zacharias, H. Spin Selectivity in Electron Transmission Through Self-Assembled Monolayers of Double-Stranded DNA. *Science* **2011**, *331*, 894–897.

- (10) Mishra, D.; Markus, T. Z.; Naaman, R.; Kettner, M.; Göhler, B.; Zacharias, H.; Friedman, N.; Sheves, M.; Fontanesi, C. Spin-Dependent Electron Transmission Through Bacteriorhodopsin Embedded in Purple Membrane. *Proc. Natl. Acad. Sci. U.S.A.* **2013**, *110*, 14872–14876.
- (11) Kettner, M.; Maslyuk, V. V.; Nürenberg, D.; Seibel, J.; Gutierrez, R.; Cuniberti, G.; Ernst, K.-H.; Zacharias, H. Chirality-Dependent Electron Spin Filtering by Molecular Monolayers of Helicenes. *J. Phys. Chem. Lett.* **2018**, *9*, 2025–2030.
- (12) Baljzović, M.; Arnoldi, B.; Grass, S.; Lacour, J.; Aeschlimann, M.; Stadtmüller, B.; Ernst, K.-H. Spin- and Angle-Resolved Photoemission Spectroscopy Study of Heptahe-licene Layers on Cu(111) Surfaces. *J. Chem. Phys.* **2023**, *159*, 044701.
- (13) Möllers, P. V.; Urban, A. J.; De Feyter, S.; Yamamoto, H. M.; Zacharias, H. Probing the Roles of Temperature and Cooperative Effects in Chirality-Induced Spin Selectivity: Photoelectron Spin Polarization in Helical Tetrapyrroles. *J. Phys. Chem. Lett.* **2024**, *15*, 9620–9629.
- (14) Badala Viswanatha, C.; Stöckl, J.; Arnoldi, B.; Becker, S.; Aeschlimann, M.; Stadtmüller, B. Vectorial Electron Spin Filtering by an All-Chiral Metal–Molecule Het-erostructure. *J. Phys. Chem. Lett.* **2022**, *13*, 6244–6249.
- (15) Möllers, P. V.; Wei, J.; Salamon, S.; Bartsch, M.; Wende, H.; Waldeck, D. H.; Zacharias, H. Spin-Polarized Photoemission from Chiral CuO Catalyst Thin Films. *ACS Nano* **2022**, *16*, 12145–12155.
- (16) Evers, F.; Aharony, A.; Bar-Gill, N.; Entin-Wohlman, O.; Hedegård, P.; Hod, O.; Jelinek, P.; Kamieniarz, G.; Lemeshko, M.; Michaeli, K. et al. Theory of Chirality Induced Spin Selectivity: Progress and Challenges. *Adv. Mater.* **2022**, *34*, 2106629.
- (17) Yeganeh, S.; Ratner, M. A.; Medina, E.; Mujica, V. Chiral Electron Transport: Scat-tering Through Helical Potentials. *J. Chem. Phys.* **2009**, *131*, 014707.

- (18) Gersten, J.; Kaasbjerg, K.; Nitzan, A. Induced Spin Filtering in Electron Transmission Through Chiral Molecular Layers Adsorbed on Metals with Strong Spin-Orbit Coupling. *J. Chem. Phys.* **2013**, *139*, 114111.
- (19) Gutierrez, R.; Díaz, E.; Gaul, C.; Brumme, T.; Domínguez-Adame, F.; Cuniberti, G. Modeling Spin Transport in Helical Fields: Derivation of an Effective Low-Dimensional Hamiltonian. *J. Phys. Chem. C* **2013**, *117*, 22276–22284.
- (20) Michaeli, K.; Naaman, R. Origin of Spin-Dependent Tunneling Through Chiral Molecules. *J. Phys. Chem. C* **2019**, *123*, 17043–17048.
- (21) Geyer, M.; Gutierrez, R.; Cuniberti, G. Effective Hamiltonian Model for Helically Constrained Quantum Systems within Adiabatic Perturbation Theory: Application to the Chirality-Induced Spin Selectivity (CISS) Effect. *J. Chem. Phys.* **2020**, *152*, 214105.
- (22) Rashba, E. I. Spin Currents in Thermodynamic Equilibrium: The Challenge of Discerning Transport Currents. *Phys. Rev. B* **2003**, *68*, 241315.
- (23) Dalum, S.; Hedegård, P. Theory of Chiral Induced Spin Selectivity. *Nano Lett.* **2019**, *19*, 5253–5259.
- (24) Fransson, J. Charge Redistribution and Spin Polarization Driven by Correlation Induced Electron Exchange in Chiral Molecules. *Nano Lett.* **2021**, *21*, 3026–3032.
- (25) Chiesa, A.; Garlatti, E.; Mezzadri, M.; Celada, L.; Sessoli, R.; Wasielewski, M. R.; Bittl, R.; Santini, P.; Carretta, S. Many-Body Models for Chirality-Induced Spin Selectivity in Electron Transfer. *Nano Lett.* **2024**, *24*, 12133–12139.
- (26) Xu, M.; Chen, Y. Enhancement of Chirality Induced Spin Selectivity by Strong Electron Correlations. *Phys. Rev. B* **2024**, *110*, 235145.
- (27) Guo, A.-M.; Sun, Q.-f. Spin-Selective Transport of Electrons in DNA Double Helix. *Phys. Rev. Lett.* **2012**, *108*, 218102.

- (28) Zhang, T.-Y.; Mao, Y.; Guo, A.-M.; Sun, Q.-F. Dynamical Theory of Chiral-Induced Spin Selectivity in Electron Donor–Chiral Molecule–Acceptor Systems. *Phys. Rev. B* **2025**, *111*, 205417.
- (29) Smorka, R.; Rudge, S. L.; Thoss, M. Influence of Nonequilibrium Vibrational Dynamics on Spin Selectivity in Chiral Molecular Junctions. *J. Chem. Phys.* **2025**, *162*, 014304.
- (30) Monti, O. L. A.; Dubi, Y. Surface Magnetic Stabilization and the Photoemission Chiral-Induced Spin-Selectivity Effect. *J. Am. Chem. Soc.* **2024**, *146*, 32795–32804.
- (31) Zöllner, M. S.; Varela, S.; Medina, E.; Mujica, V.; Herrmann, C. Insight into the Origin of Chiral-Induced Spin Selectivity from a Symmetry Analysis of Electronic Transmission. *J. Chem. Theory Comput.* **2020**, *16*, 2914–2929.
- (32) Zöllner, M. S.; Saghatchi, A.; Mujica, V.; Herrmann, C. Influence of Electronic Structure Modeling and Junction Structure on First-Principles Chiral Induced Spin Selectivity. *J. Chem. Theory Comput.* **2020**, *16*, 7357–7371.
- (33) Naskar, S.; Mujica, V.; Herrmann, C. Chiral-Induced Spin Selectivity and Non-equilibrium Spin Accumulation in Molecules and Interfaces: A First-Principles Study. *J. Phys. Chem. Lett.* **2023**, *14*, 694–701.
- (34) Day, P. N.; Pachter, R.; Nguyen, K. A.; Hong, G. Chirality-Induced Spin Selectivity: Analysis of Density Functional Theory Calculations. *J. Chem. Theory Comput.* **2024**, *20*, 5475–5486.
- (35) Gutierrez, R.; Díaz, E.; Naaman, R.; Cuniberti, G. Spin-Selective Transport Through Helical Molecular Systems. *Phys. Rev. B* **2012**, *85*, 081404.
- (36) Wolf, Y.; Liu, Y.; Xiao, J.; Park, N.; Yan, B. Unusual Spin Polarization in the Chirality-Induced Spin Selectivity. *ACS Nano* **2022**, *16*, 18601–18607.

- (37) Hüfner, S. *Photoelectron Spectroscopy: Principles and Applications*, 3rd ed.; Springer: Berlin, 2003.
- (38) Damascelli, A.; Hussain, Z.; Shen, Z.-X. Angle-Resolved Photoemission Studies of the Cuprate Superconductors. *Rev. Mod. Phys.* **2003**, *75*, 473–541.
- (39) Liu, Z.-F. Many-Body Effects at Heterogeneous Interfaces from First-Principles: Progress, Challenges, and Opportunities. *ACS Nano* **2025**, *19*, 5861–5870.
- (40) Wang, Y. H.; Hsieh, D.; Pilon, D.; Fu, L.; Gardner, D. R.; Lee, Y. S.; Gedik, N. Observation of a Warped Helical Spin Texture in  $\text{Bi}_2\text{Se}_3$  from Circular Dichroism Angle-Resolved Photoemission Spectroscopy. *Phys. Rev. Lett.* **2011**, *107*, 207602.
- (41) Park, C.-H.; Louie, S. G. Spin Polarization of Photoelectrons from Topological Insulators. *Phys. Rev. Lett.* **2012**, *109*, 097601.
- (42) Borstel, G.; Wöhlecke, M. Spin Polarization of Photoelectrons Emitted from Nonmagnetic Solids. *Phys. Rev. B* **1982**, *26*, 1148–1155.
- (43) Borstel, G.; Wöhlecke, M. Theoretical Study of Electron-Spin Polarization in Photoemission from Au surfaces. *Surf. Sci.* **1982**, *117*, 310–318.
- (44) Wöhlecke, M.; Borstel, G. In *Optical Orientation*; Meier, F., Zakharchenya, B. P., Eds.; Modern Problems in Condensed Matter Sciences; Elsevier: Amsterdam, 1984; Vol. 8; pp 423–462.
- (45) Duhm, S.; Gerlach, A.; Salzmann, I.; Bröker, B.; Johnson, R.; Schreiber, F.; Koch, N. PTCDA on Au (111), Ag (111) and Cu (111): Correlation of Interface Charge Transfer to Bonding Distance. *Org. Electron.* **2008**, *9*, 111–118.
- (46) LaShell, S.; McDougall, B. A.; Jensen, E. Spin Splitting of an Au(111) Surface State Band Observed with Angle Resolved Photoelectron Spectroscopy. *Phys. Rev. Lett.* **1996**, *77*, 3419–3422.

- (47) Petersen, L.; Hedegård, P. A Simple Tight-Binding Model of Spin–Orbit Splitting of *sp*-Derived Surface States. *Surf. Sci.* **2000**, *459*, 49–56.
- (48) Ärrälä, M.; Nieminen, J.; Braun, J.; Ebert, H.; Lindroos, M. Photon Energy Dependence of Circular Dichroism of the Au(111) Surface State. *Phys. Rev. B* **2013**, *88*, 195413.
- (49) Perdew, J. P.; Burke, K.; Ernzerhof, M. Generalized Gradient Approximation Made Simple. *Phys. Rev. Lett.* **1996**, *77*, 3865–3868.
- (50) Neaton, J. B.; Hybertsen, M. S.; Louie, S. G. Renormalization of Molecular Electronic Levels at Metal-Molecule Interfaces. *Phys. Rev. Lett.* **2006**, *97*, 216405.
- (51) Hybertsen, M. S.; Louie, S. G. Electron Correlation in Semiconductors and Insulators: Band Gaps and Quasiparticle Energies. *Phys. Rev. B* **1986**, *34*, 5390–5413.
- (52) Deslippe, J.; Samsonidze, G.; Strubbe, D. A.; Jain, M.; Cohen, M. L.; Louie, S. G. BerkeleyGW: A Massively Parallel Computer Package for the Calculation of the Quasiparticle and Optical Properties of Materials and Nanostructures. *Comput. Phys. Commun.* **2012**, *183*, 1269–1289.
- (53) Braun, J. The Theory of Angle-Resolved Ultraviolet Photoemission and Its Applications to Ordered Materials. *Rep. Prog. Phys.* **1996**, *59*, 1267–1338.